

# Determination of RMS Current Load on the DC-link Capacitor of Voltage Source Converters using Direct Current Control

Sebastian Raab, Andreas Krämer and Ansgar Ackva  
 University of Applied Sciences Würzburg-Schweinfurt  
 TTZ-EMO - Technology Transfer Centre for E-mobility  
 Poststraße 31, 97616 Bad Neustadt a. d. Saale, Germany

Email: Sebastian.Raab@fhws.de, Andreas.Kraemer@fhws.de, Ansgar.Ackva@fhws.de

**Abstract**—RMS current load is one of the most important design criteria for the DC-link capacitors of voltage source converters. In literature, determination of this RMS current load is well documented for state-of-the-art modulation schemes like space vector modulation. But the methods presented can not be applied for direct current control algorithms. Therefore, the paper introduces a new approach specially for direct current controllers which reflects and compares to the state-of-the-art calculation method for space vector modulation. As direct current control is a feedback control, no closed-form solution can be given. Instead, the DC-link capacitor RMS current load is determined by an iterative calculation scheme as a function of the modulation level and the phase angle. Although the scheme presented is applied to a three phase two level voltage source converter it can be adapted to any voltage source converter topology. An example is presented applying the calculation method to one specific direct current control algorithm. The calculated results are verified via a digital simulation model as well as test bench measurements showing good correlation. For correct comparison, different effects are considered and discussed between simulation, calculation and measurement results. These contain transients, the commutation process between IGBT and Diode, the current dependent voltage drop of the semiconductors and the stationary current error of the hysteresis control. The DC-link capacitor current load for space vector modulation is calculated analytically as a reference by using the state-of-the-art method. The comparison of results obtained in this paper and the reference are very similar which is discussed in the conclusion.

## I. INTRODUCTION

In industrial as well as automotive drive trains, two-level voltage source converters (VSCs) can be considered as state-of-the-art technology. For proper operation of VSCs, their DC voltage needs to be stabilized by the use of capacitors. The kind of capacitor strongly depends on the application. For example in automotive traction drive trains, efforts are made in lowering the capacitors footprint and costs which cause 14% to 16% of the total costs of the traction drive VSC [1]. For

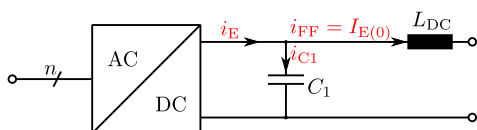


Figure 1: Voltage source converter with DC-link capacitor.

correct capacitor specification, the current load  $I_{C1}$  as well as the capacitor ripple voltage  $U_{C1\sim}$  have to be determined precisely.

In [2] a method for the analytical calculation of DC-link capacitor current load is described by means of a space vector modulation (SVM) controlled VSC. For this purpose, the root mean square (RMS) value of the distortion current at the VSCs DC-side  $I_{E\sim}$  is a valid measure.  $I_{E\sim}$ , often called the ripple current, is determined from the RMS value  $I_E$  and its DC component  $I_{E(0)}$  according to (1). Assuming ideal filtering given for the conditions in (2),  $I_{E\sim}$  can be interpreted as  $I_{C1}$ .

$$I_{E\sim} = \sqrt{I_E^2 - I_{E(0)}^2} \quad (1)$$

$$I_{E\sim} = I_{C1} \text{ for } \omega L_{DC} \gg \frac{1}{\omega C_1} \quad (2)$$

Equation (1) can be applied to various pulse width modulation schemes. Literature can be found where  $I_{E\sim}$  is also used to determine the DC-link capacitor current load for interleaved VSC systems, see [3]. In [4], the normalized distortion current load factor of the DC-link is defined as given in (3).

$$K_{DC} = \frac{I_{E\sim}^2}{I_n^2} \text{ with } n = U, V, W \quad (3)$$

$I_n$  represents the RMS values of the VSCs 3-phase AC-side currents. The RMS values of the phase currents are assumed to be equal, so  $I_n = I_N$ .

In [4], it is shown that the unit-less distortion current load factor  $K_{DC}$  is independent of the AC current. It only depends on the modulation level  $m_a$  and the phase displacement angle  $\varphi$ . Therefore, it is suitable for comparing the impact of different modulation as well as direct control methods on the DC-link capacitor current load [5], [6]. In [7],  $K_{DC}$  is applied and calculated for the reduced common mode voltage PWM (RCMPWM), a PWM technique specifically developed to alleviate common mode voltages.

In Fig. 2,  $K_{DC}$  for SVM is shown depending on  $m_a$  defined by (4) and  $\varphi$ . Here,  $\hat{u}_{n(1)}$  with  $n = U, V, W$  describes the amplitude of the VSC neutral point output voltage  $u_n$  at fundamental frequency.

$$m_a = \frac{2\hat{u}_{n(1)}}{u_{C1}} \quad (4)$$

Since SVM is the most widely used modulation method for VSCs, the calculated characteristic values are subsequently used as a reference for comparison.

The capacitor ripple voltage  $U_{C1\sim}$  can also be determined analytically for SVM according to [8]. The general solution is given in (5).

$$\begin{aligned} U_{C1\sim} &= \sqrt{\frac{3}{\pi} \int_{\varphi_U}^{\varphi_U + \pi/3} U_{C1\sim,TP} d\varphi_U} \\ U_{C1\sim,TP}^2 &= \frac{1}{T_P} \int_0^{T_P} u_{C1\sim}^2 dt \\ u_{C1\sim} &= \frac{1}{C_1} \int I_{E(0)} - i_E dt \end{aligned} \quad (5)$$

So, the knowledge of  $i_{E\sim}$  in every operation point is fundamental for dimensioning of the DC-link capacitor because current load as well as ripple voltage can be derived from it.  $i_{E\sim}$  in turn depends on the switching timings of the VSC.

In sections II and III, a method to calculate  $I_{E\sim}$  for direct current controlled VSCs is described step by step:

- II Direct current control is introduced. Its different switching conditions in comparison to SVM are declared using an exemplary direct current control method called Scalar Hysteresis Control (SHC).
- III A calculation method for the total switch-on times is given for SHC.
  - B The relative switch-on times are derived from the total switch-on times proving the calculation method presented is hardware independent. Therefore, the expression „pulse group“ with duration  $t_{PG}$  is established.
  - C  $I_{E\sim}$  is calculated for SHC, depending only on modulation level  $m_a$  and phase displacement angle  $\varphi$ .

## II. DIRECT CURRENT CONTROL

The aim of any feedforward modulation method mentioned in section I is the generation of pulse-patterns for setting the target voltage  $u_n^*$  with  $n = U, V, W$  given by a higher-levelled controller. In many applications, this higher-levelled controller is used to tune the AC current. Due to this

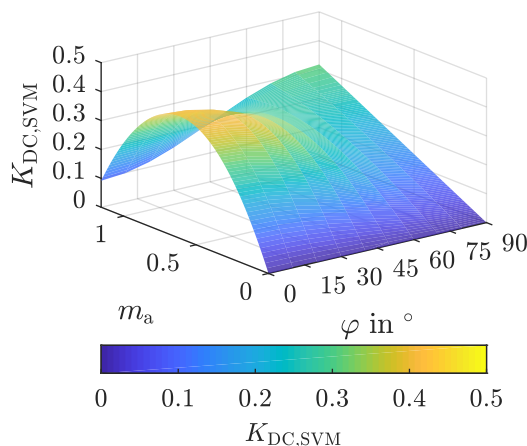


Figure 2: Normalized distortion current load factor of the DC-link for SVM.

architecture, these methods are also referred as indirect current control. In contrast, for direct current control, the set current  $i^*$ , the measured current  $i$  and the fundamental voltage at the VSC AC-side are taken into account for directly triggering a switching action in order to keep the current error  $i_\epsilon$  inside a predefined tolerance area.

### A. Hysteresis Control

A well known direct current control method is the two-point hysteresis control [9]<sup>1</sup>. A tolerance area for the current error  $i_{\epsilon,n}$  in phase  $n$ , consisting of an upper limit  $I_{\epsilon,high}$  and a lower limit  $I_{\epsilon,low}$  is defined (see eq. (6)). For the three phase two-point hysteresis controller, the current error  $i_{\epsilon,n}$  is calculated separately in each phase of the VSC according to (6). If  $i_{\epsilon,n}$  exceeds the limits of the tolerance area, a switching action defined in (7) is triggered. Therefore, a switch position is selected, which reduces the current error in the corresponding phase. The output voltage  $u_n$  is defined in (8).

$$i_{\epsilon,n} = i_n - i_n^*, \text{ for } n = U, V, W \quad (6)$$

$$s_n = \begin{cases} +1, & \text{for } i_{\epsilon,n} > I_{\epsilon,high} \\ -1, & \text{for } i_{\epsilon,n} < I_{\epsilon,low} \end{cases} \quad (7)$$

$$u_n = s_n \frac{u_{C1}}{2} \quad (8)$$

For three-phase VSCs, in the most simple case, all three phase currents are regulated independently from each other. However, this leads to an over-determination of the system in case of a non-connected neutral point.

For control reasons, the current error for three-phase applications can be converted into the  $\alpha\beta$ -system by means of Clarke transformation to solve the mentioned issue of over-determination [10].

### B. Relation Between Voltage and Current Vector

Hereafter, the voltage as well as the current are described in the  $\alpha\beta$ -system for the three-phase direct current control methods. In Fig. 3, the relationship between voltage  $\underline{u}'_{\alpha\beta}$ , set current  $\hat{i}_{\alpha\beta}^*$  and measured current  $\hat{i}_{\alpha\beta}$  are shown. The vector  $\underline{u}'_{\alpha\beta}$  represents the mean value of the VSC output voltage normalized to the intermediate circuit voltage  $u_{C1}$ . It is defined in (9).

$$\begin{aligned} \underline{u}'_{\alpha\beta} &= |\underline{u}'_{\alpha\beta}| (\cos(\varphi_U) + j \sin(\varphi_U)) \\ \text{with } |\underline{u}'_{\alpha\beta}| &= \frac{1}{2} m_a = \frac{\hat{u}_n(1)}{u_{C1}} \\ \text{and } \varphi_U &= \arg(\underline{u}'_{\alpha\beta}) = \int 2\pi f dt \end{aligned} \quad (9)$$

The current  $\hat{i}_\epsilon$  describes the current error, defined in (10). In the example representation in Fig. 3, the tolerance area is drawn as a circle with radius  $I_\epsilon$ , but may take different forms depending on the control method used. For example in [11], the tolerance area forms a square using three active space vectors (SV) and the zero voltage vectors (ZVV) to control  $\hat{i}_{\alpha\beta}$ .

$$\hat{i}_\epsilon = \hat{i}_{\alpha\beta} - \hat{i}_{\alpha\beta}^* \quad (10)$$

<sup>1</sup>page 205 et seq.

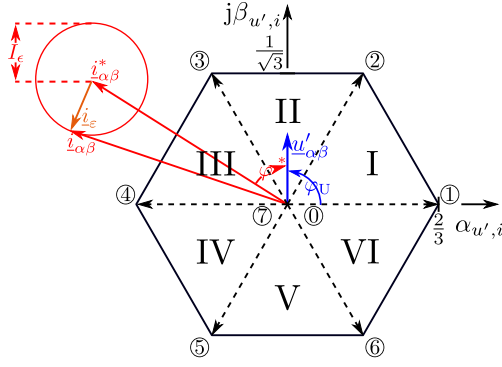


Figure 3: Graphical illustration of the relationship between normalized voltage and current phasors in the  $\alpha\beta$  plane. Tolerance circle for Scalar Hysteresis Control (SHC).

### C. Scalar Hysteresis Control (SHC)

The SHC method presented in [12] represents the development of a relative new direct current controller. Only those two SVs adjacent to  $\underline{u}'_{\alpha\beta}$  as well as the ZVV are used to control the current  $\underline{i}_{\alpha\beta}$  under steady-state conditions<sup>2</sup>. The areas with identical SVs form triangles and define the limits of the voltage sectors I to VI.

The individual SVs are determined by evaluating the vector of the current error  $\underline{i}_{\epsilon}$  in the alpha-beta plane (see Fig. 3). For the maximum of  $\underline{i}_{\epsilon}$ , a tolerance circle with radius  $I_{\epsilon}$  is defined as shown in Fig. 3. Once the limit of this area is exceeded, a switching operation is triggered and the SV is selected which best moves  $\underline{i}_{\epsilon}$  back into the circle [13]. Equations (11) and (12) describe the vector choice for the exemplary case of voltage sector II with  $\pi/3 \leq \varphi_U \leq 2\pi/3$ .

$$k = \arg \min_{k=0,2,3} \Re((\underline{u}'_{SVk} - \underline{u}'_{\alpha\beta}) \bar{\underline{i}}_{\epsilon}) \quad (11)$$

$$\begin{aligned} \underline{u}'_{SV0} &= 0 \\ \underline{u}'_{SV2} &= \frac{2}{3} e^{j\pi/3} \\ \underline{u}'_{SV3} &= \frac{2}{3} e^{j2\pi/3} \end{aligned} \quad (12)$$

In order to compare the DC ripple current for this direct current controller type with SVM, the distortion current load factor  $K_{DC,SHC}$  has to be determined as a function of modulation level and phase angle. For the calculation of the RMS value of the distortion current  $I_{E\sim}$  at first the general approach for SVM presented in [2] is chosen and adapted to the attributes of direct current control.

### III. CALCULATION OF RMS CURRENT LOAD ON THE DC-LINK CAPACITOR

At first, an adapted generic form of the approach in [2] is given. The RMS value as well as the DC component of  $i_E$  are calculated from the switching functions  $s_{SVx,n}$  and  $s_{SVy,n}$  as well as from the AC-currents  $i_n$ . This calculation shown in (13) results the RMS value of the DC-side distortion current

<sup>2</sup>For dynamic operations a second, greater tolerance area is defined.

over one pulse period  $I_{E\sim,TP}$  with duration  $T_P$ . The variables  $\delta_x$  and  $\delta_y$  represent the relative on times of the SV's x and y during one switching period.

Due to geometrical issues, the RMS value of  $I_{E\sim,TP}$  over one arbitrary voltage sector results the global RMS value of the DC-side distortion current  $I_{E\sim}$  shown in (14). Indices x and y correspond to the name of the active SV's used to emulate the voltage vector  $\underline{u}_{\alpha\beta}$ .

$$\begin{aligned} I_{E\sim,TP}^2 &= \left( \delta_x(\varphi_U) \sum_{n=U,V,W} \left( \frac{s_{SVx,n} - 1}{2} \cdot i_n^2 \right) \right. \\ &+ \delta_y(\varphi_U) \sum_{n=U,V,W} \left( \frac{s_{SVy,n} - 1}{2} \cdot i_n^2 \right) \\ &- \left( \delta_x(\varphi_U) \sum_{n=U,V,W} \left( \frac{s_{SVx,n} - 1}{2} \cdot i_n \right) \right. \\ &\left. \left. + \delta_y(\varphi_U) \sum_{n=U,V,W} \left( \frac{s_{SVy,n} - 1}{2} \cdot i_n \right) \right)^2 \end{aligned} \quad (13)$$

$$I_{E\sim}^2 = \frac{3}{\pi} \int_{\Phi_U}^{\Phi_U + \pi/3} I_{E\sim,TP}^2 d\varphi_U \quad (14)$$

Due to the mentioned switching vector selection for the SHC method taking into account only the two adjacent SVs as well as the ZVV, the parameters required for the calculation of (14) can be determined. For voltage sector II, the general switching functions  $s_{SVx,n}$  and  $s_{SVy,n}$  can be substituted:

$$\begin{aligned} s_{SVx,n} &= s_{SV3,n} = [-1 + 1 - 1] \\ s_{SVy,n} &= s_{SV2,n} = [+1 + 1 - 1] \end{aligned} \quad (15)$$

With (15), the general form given in (13) can be simplified:

$$I_{E\sim,TP}^2 = \delta_3 i_V^2 + \delta_2 i_W^2 - (\delta_3 i_V - \delta_2 i_W)^2 \quad (16)$$

The fundamentals of the phase currents  $i_n$  are defined according to (17) with amplitude  $\hat{I}_N$  and phase displacement angle  $\varphi$ .

$$\begin{aligned} i_{U(1)} &= \hat{I}_N \cos(\varphi_U - \varphi) \\ i_{V(1)} &= \hat{I}_N \cos(\varphi_U - \frac{2\pi}{3} - \varphi) \\ i_{W(1)} &= \hat{I}_N \cos(\varphi_U + \frac{2\pi}{3} - \varphi) \end{aligned} \quad (17)$$

If the limit of the tolerance area is violated, a new SV is selected and applied until the AC-side distortion current  $\underline{i}_{\epsilon}$  again exceeds the tolerance area. Thus, the duration of the SV is dependent on the travel speed of  $\underline{i}_{\epsilon}$ , i.e. the current slope  $d\underline{i}_{\epsilon}/dt$ .

The upper part of the equivalent circuit diagram in Fig. 4 describes the VSC AC-side considering the load voltage  $e_{\alpha\beta}$ , the load impedance  $L_L$  and  $R_L$  as well as the filter impedance  $L_N$  and  $R_N$ . With  $L_N \gg L_L$  the distortion of the VSC output voltage  $\underline{u}_{SV}$  is set equal to the voltage  $\underline{u}_{L\epsilon}$ . So, it becomes clear that the current slope is related to  $\underline{u}_{L\epsilon}$ . The lower part describes the VSC DC-side considering the DC voltage source  $u_{DC}$ , the DC line impedance  $L_{DC}$  and  $R_{DC}$  as well as the DC-link capacitor  $C_1$ .  $I_{E(0)}$  represents the DC component of the VSC DC-side input current,  $i_{E\sim}$  its distortion.

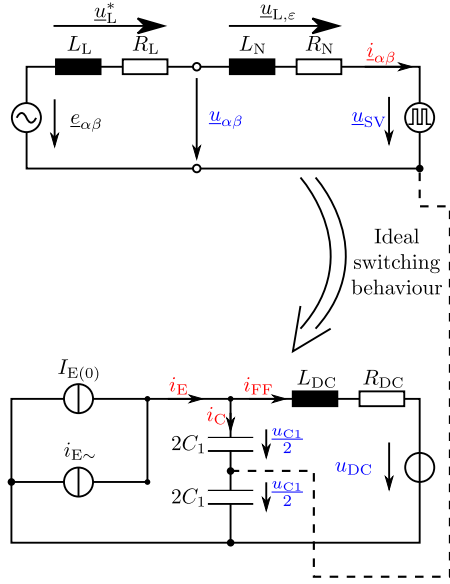


Figure 4: Equivalent circuit diagram of the DC (bottom) and AC (top) side of a VSC, assuming ideal sinusoidal output voltage  $\underline{u}_{\alpha\beta}$  and reverse voltage  $\underline{e}_{\alpha\beta}$ .

#### A. Determination of on times

For the computation of the on time  $t_{SV}$  between one violation of the tolerance area at time  $t_0$  and the subsequent at  $t_1$ , the course of  $\underline{i}_\varepsilon$  has to be determined. For the calculations presented it is assumed that:

- The voltage  $\underline{u}_{L\varepsilon}$  is only applied to the inductance  $L_N$ , i.e.  $R_N = 0 \Omega$ .
- The reverse voltage  $\underline{e}_{\alpha\beta}$  during the on time of a SV is constant. Thus, the current slope for a switching state can be assumed to be constant.

In [14] a method for the computation of  $\underline{i}_\varepsilon(t)$  depending on the selected SV is introduced and used for predictive current control. This method can subsequently be applied to determine  $t_{SV}$ .

Provided that  $t_{SV}$  is defined by:

$$t_{SV} = t_1 - t_0 \quad (18)$$

The current error is already defined in (10). At time  $t_1$ ,  $\underline{i}_\varepsilon$  hits the limit of the tolerance area again. This represents the necessary criterion for triggering a new switching action.

The following relations (19), (20) and (21) describe the course of the square of the current error magnitude  $i_\varepsilon^2$ . These relations as well as the auxiliary quantities  $a_1$  and  $a_2$  are taken from [14]. Here, the current error vector  $\underline{i}_\varepsilon$  is divided into its real component  $i_{\varepsilon,\alpha}$  and its imaginary component  $i_{\varepsilon,\beta}$ . The same is done with the current slope vector  $\frac{di_\varepsilon}{dt}$ .

$$i_\varepsilon^2(t_1) = i_\varepsilon^2(t_0) - a_1(t_0) \cdot (t_1 - t_0) + a_2(t_0) \cdot (t_1 - t_0)^2 \quad (19)$$

$$a_1(t_0) = 2 \left( i_{\varepsilon,\alpha}(t_0) \cdot \frac{di_{\varepsilon,\alpha}}{dt}(t_0) + i_{\varepsilon,\beta}(t_0) \cdot \frac{di_{\varepsilon,\beta}}{dt}(t_0) \right) \quad (20)$$

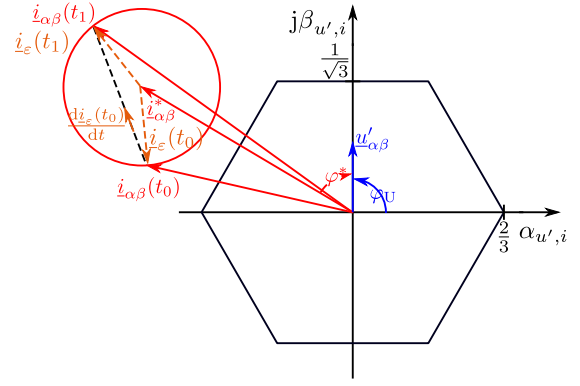


Figure 5: Calculated course of the current error using the approach presented in [14].

$$a_2(t_0) = \left( \frac{di_{\varepsilon,\alpha}}{dt}(t_0) \right)^2 + \left( \frac{di_{\varepsilon,\beta}}{dt}(t_0) \right)^2 \quad (21)$$

Depending on the selected SV, the chronological sequence of the current  $\underline{i}_\varepsilon(t)$  can take any secant of the error circle with radius  $I_\varepsilon$ . To determine  $\underline{i}_\varepsilon(t)$  the slope of  $\underline{i}_\varepsilon(t)$  is calculated for  $t = t_0$  as shown in (22). It indicates the absolute value and the direction of the chronological sequence of  $\underline{i}_\varepsilon(t)$  for  $t_0 \leq t < t_1$ .

$$\frac{di_\varepsilon}{dt}(t_0) = \frac{u_{L\varepsilon}}{L_N} \quad (22)$$

After expiration of  $t_{SV}$  the current error reaches the limit of the tolerance area and a new SV needs to be selected and applied. The resulting quadratic function (19) provides information about the number of possible solutions for  $t_1$ . A detailed calculation of  $t_{SV}$  is given in equations (23), (24) and (25). The results coincide with [14].

General solution for  $t_{1,1/2}$ :

$$t_{1,1/2} = \frac{2a_2(t_0)t_0 - a_1(t_0) \pm \sqrt{d}}{2a_2(t_0)} \quad (23)$$

Provided that discriminant  $d$  is covered by:

$$d = a_1^2(t_0) + 4a_2(t_0)I_\varepsilon^2 - 4a_2(t_0)i_\varepsilon^2(t_0) \quad (24)$$

Special solution for  $i_\varepsilon^2(t_0) = i_\varepsilon^2(t_1) = I_\varepsilon^2$ :

$$t_{1,1/2} = \frac{2a_2(t_0)t_0 - a_1(t_0) \pm a_1(t_0)}{2a_2(t_0)}$$

$$\text{Solution 1: } t_1 = t_0 \Rightarrow t_{SV} = 0 \quad (25)$$

$$\text{Solution 2: } t_1 = t_0 - \frac{a_1}{a_2} \Rightarrow t_{SV} = -\frac{a_1}{a_2}$$

$$\text{with } t_{SV} = t_1 - t_0$$

Using the determined on time and the calculated current slope, the current error for  $t = t_1$ , when  $\underline{i}_\varepsilon$  again exceeds the limit of the tolerance area, can be calculated by (26).

$$\begin{aligned} \underline{i}_\varepsilon(t_1) &= \underline{i}_\varepsilon(t_0) + \Delta \underline{i}_\varepsilon \\ \text{with } \Delta \underline{i}_\varepsilon &= \frac{d\underline{i}_\varepsilon}{dt}(t_0) \cdot t_{SV} \\ \Delta \underline{i}_\varepsilon &= -\frac{2i_{\varepsilon,\alpha}(t_0)u_{L\varepsilon,\alpha} + 2i_{\varepsilon,\beta}(t_0)u_{L\varepsilon,\beta}}{u_{L\varepsilon,\alpha}^2 + u_{L\varepsilon,\beta}^2} \underline{u}_{L\varepsilon} \end{aligned} \quad (26)$$

Using (26),  $\underline{i}_\varepsilon(t_1)$  is recalculated iteratively to reconstruct the course of  $\underline{i}_\varepsilon(t)$  over any number of switching operations as shown in (27). The starting point for the very first calculation  $\underline{i}_\varepsilon(t_{m-1})$  at  $m = 1$  is set to an arbitrary point at the limits of the tolerance area.

$$\underline{i}_\varepsilon(t_m) = \underline{i}_\varepsilon(t_{m-1}) + \frac{d\underline{i}_\varepsilon}{dt}(t_{m-1}) \cdot t_{SVm} \quad (27)$$

$$\forall \{m \in \mathbb{N}\}$$

The on times  $t_{SVm}$  can also be calculated iteratively according to (28).

$$t_{SVm} = -2L_N \frac{i_{\varepsilon,\alpha} u_{L\varepsilon,\alpha} + i_{\varepsilon,\beta} u_{L\varepsilon,\beta}}{u_{L\varepsilon,\alpha}^2 + u_{L\varepsilon,\beta}^2} \quad (28)$$

### B. Pulse Groups

To determine the relative on times  $\delta_x$  and  $\delta_y$  the period duration must be determined first. Indirect control procedures have a fixed pulse period duration  $T_P$ . It represents the time between two identical sequences of space vectors, provided that the relative switch-on time of the vectors is variable.

Direct current control methods do not have such a fixed pattern of identical sequences. Therefore, the term period duration cannot be used. However, in order to form the ratio of the on times of successive space vectors  $t_{SVm}$ , these are combined into a pulse group with duration  $t_{PG}$ . The number of vectors a pulse group contains is defined equal to the number of space vectors available within the considered voltage sector and is denoted with  $M$ .

$$t_{PG}(\varphi_U) = \sum_{m=1}^M t_{SVm} \quad (29)$$

For SHC,  $M = 3$ . This means,  $t_{PG}$  is calculated according to (29) summing up three successive calculations of  $t_{SVm}$  that create a pulse group.

For the considered example of voltage sector II from Fig. 3, the relative on times  $\delta_2(\varphi_U)$  and  $\delta_3(\varphi_U)$  needed for solving (16) are redefined as the ratios between total on times of equal active space vectors in one pulse group and  $t_{PG}$ . In (30), the relative on time  $\delta_2$  is calculated exemplarily from the absolute on time  $t_2$  defined in (31).  $\delta_3$  is determined analogously. In (31), the absolute on time  $t_2$  for one pulse group is calculated iteratively using the switching criterion  $k$  of the SHC given in (11).  $k$  defines the decision criterion which voltage space vector is set to reduce the current error. It is recalculated step by step. i.e. for every step  $m$  that represents a violation of the current-tolerance area.

$$\delta_2(\varphi_U) = \frac{t_{SV2}(\varphi_U)}{t_{PG}(\varphi_U)} \quad (30)$$

$$t_{SV2}(\varphi_U) = \sum_{m=1}^M t_{SVm} \forall \{m | k(m) = 2\} \quad (31)$$

Substituting  $t_{SVm}$  in (29) and (31) by means of (28) and inserting the expressions in (30), it can be seen that  $\delta_2(\varphi_U)$  is independent of  $L_N$ . Therefore, the voltage  $\underline{u}_{L\varepsilon}$  can be substituted by the unit-less variable  $\underline{u}'_{L\varepsilon}$  which can be determined

according to (32). As  $|\underline{i}_\varepsilon(t_m)| = |\underline{i}_\varepsilon(t_{m-1})|$ ,  $\delta_2(\varphi_U)$  is also independent of  $I_\varepsilon$  as long as  $I_\varepsilon > 0$  A. This proves, the method presented is hardware independent.

$$\underline{u}'_{L\varepsilon} = \underline{u}'_{\alpha\beta}(\varphi_U) - \underline{u}'_{SVk} \quad (32)$$

In (14),  $\varphi_U$  is assumed to be constant during the pulse period duration  $T_P$ . This assumption is also made for the pulse group duration  $t_{PG}$ . Now, the RMS value of the distortion current over one pulse group  $i_{E\sim,t_{PG}}$  can be calculated analogously to (16) by substituting  $T_P$  with  $t_{PG}$  as shown in (33).

$$i_{E\sim,t_{PG}}^2(\varphi_U) = \delta_3 i_V^2 + \delta_2 i_W^2 - (\delta_3 i_V - \delta_2 i_W)^2 \quad (33)$$

### C. Calculation of the global RMS value

To calculate the global RMS value of the distortion current  $I_{E\sim}$ , the RMS value of  $i_{E\sim,t_{PG}}$  for one arbitrary sector is calculated. For the iterative algorithm presented, the integral in (14) can not be solved analytically. Therefore, it is solved numerically, using the step size  $\Delta\Phi_U$  and the number of steps  $G$  according to (34).

$$I_{E\sim}^2 = \frac{1}{G} \sum_{g=0}^G i_{E\sim,t_{PG}}^2(\Phi_U + g\Delta\Phi_U) \quad (34)$$

$$\Delta\Phi_U = \frac{\pi}{3G} \forall \{G \in \mathbb{N}\}$$

Assuming  $\varphi_U$  to be constant during the pulse group duration  $t_{PG}$ ,  $\varphi_U$  is recalculated for every pulse group. The course of  $\underline{i}_\varepsilon(t_m)$  is calculated iteratively for  $0 \leq g \leq G$ . Therefore, a case-differentiation for its starting point at  $m = 1$  needs to be defined according to (35).

$$\underline{i}_\varepsilon(t_m, \varphi_U) = \underline{i}_\varepsilon(t_{m-1}, \varphi_U) + \frac{d\underline{i}_\varepsilon}{dt}(t_{m-1}) \cdot t_{SVm} \quad (35)$$

$$\underline{i}_\varepsilon(t_0, \varphi_U) = \begin{cases} I_\varepsilon e^{j0} & \varphi_U = \Phi_U \\ \underline{i}_\varepsilon(t_M, \varphi_U - \Delta\Phi_U) & \varphi_U > \Phi_U \end{cases}$$

The precision of this solution depends on the choice of the step size  $\Delta\Phi_U$ . For the results presented, the number of steps is set to  $G = 100$  resulting in  $\Delta\Phi_U = \pi/300$ . Using the given relations, the distortion current load factor  $K_{DC,SHC}$  can be calculated. A comparison of  $K_{DC,SHC}$  and  $K_{DC,SVM}$  is shown in Fig. 6.

## IV. VERIFICATION OF THE RESULTS USING DIGITAL SIMULATION

To verify the calculated results from III, a digital simulation model was created. Fig. 7 shows the comparison results for  $0 < m_a \leq 2/\sqrt{3}$  and  $\varphi = 0^\circ$ .

- Calculation method presented: Curve  $K_{DC,SHC,calc}$ .
- Simulation model accounting current commutation of the VSC: Curve  $K_{DC,SHC,sim}$ .

The comparison shows good correlation between simulation and calculation. For  $m_a \rightarrow 0$  the shape of the curve  $K_{DC,SHC,calc}$  deviates from  $K_{DC,SHC,sim}$ . This deviation can be addressed to the current commutation.

Calculation does not take into account the current commutation process and the delay time  $t_D$  it takes switching from one

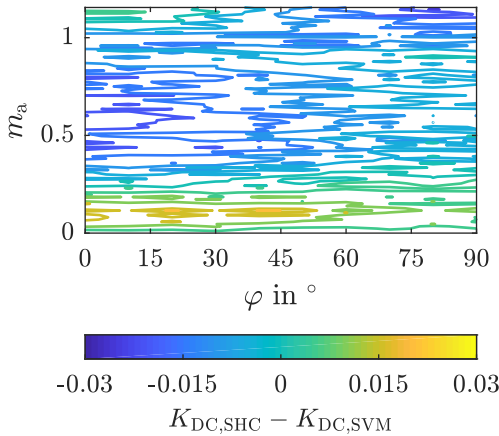


Figure 6: Distortion current load factor when using the SHC method in comparison to the SVM used as a reference.

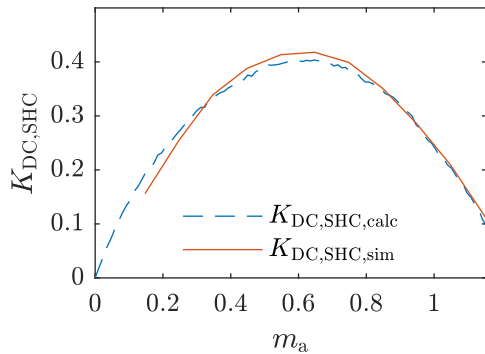


Figure 7: Comparison of simulation and calculated results for the distortion current load factor using SHC.

SV to another. This time delays the switch-on timing of the SV in comparison to the switch-on command from the SHC. Until the time  $t_D$  has elapsed, the SHC sends no further switching commands to the VSC. This ensures that the minimum on time of a SV is set to  $t_D$ . As this issue also arises when comparing calculated results with experimental results, a more detailed analysis is given in section V-B.

## V. EXPERIMENTAL RESULTS

To verify the calculated and the simulative results, the VSC DC-side current  $i_E$  is measured on an experimental set-up. Fig. 8 shows a schematic of the test bench. The device under test (DUT) is a three-phase IGBT power module. To absorb the distortion current, the electrolytic capacitor  $C_1$  and three snubber capacitors  $C_{S,n}$  are used. The AC-side output voltage is filtered by the inductances  $L_n$ . To generate a sinusoidal load voltage, a power grid simulator is used. For providing the constant DC voltage, a DC source/sink is applied to the test bench. The amplitude of the three phase AC-side load voltages of the power grid simulator  $\hat{e}_N$  is varied to adjust different modulation levels. As the current setpoint is kept constant, the power handled by the VSC varies from 630 VA at  $m_a = 0.1$  to 7000 VA at  $m_a = 1.15$ . Parameters of the hardware set-up are given in Tab. I.

Table I: Parameters of hardware set-up for test bench, with  $n = U, V, W$ .

Current setpoint	$\hat{I}_N^*(50 \text{ Hz}) = 20 \text{ A}$
Grid filter	$L_n(100 \text{ Hz}) = 1,2 \text{ mH}$ $R_n = 1 \text{ m}\Omega$
Copper Rails	$Z_{R,n}(100 \text{ Hz}) =$ $0,1 \text{ m}\Omega + j\omega 140 \text{ nH}$
Snubber capacitors	$C_{S,n}(100 \text{ Hz}) = 470 \text{ nF}$
Connection plate	$Z_P(100 \text{ Hz}) =$ $0,24 \text{ m}\Omega + j\omega 250 \text{ nH}$
DC-link capacitor	$C_1(100 \text{ Hz}) = 4,6 \text{ mF}$
DC Coupling	$L_{DC1}(100 \text{ Hz}) = 34,5 \mu\text{H}$
DC-link voltage	$U_{DC(0)} = 300 \text{ V}$

In order to achieve a low inductance connection between the DC-link capacitor and the DUT, the DC bus bar is bolted directly on the half bridge modules including three snubber foil capacitors. The DC current  $i_E$  describes the sum of three half bridge DC currents  $i_{DC,n}$ . To measure  $i_E$  correctly, the current sensors are placed in between the DUT and the snubber capacitors as shown in Fig. 8. This is done because the currents  $i_{S,n}$  of the snubber capacitors  $C_{S,n}$  significantly influence the measurements. For this purpose, U-formed copper rails with impedance  $Z_{R,n}$  are inserted between the DC connection point of the three half bridges and the snubber capacitors as shown in Fig. 9. The impedance of the DC bus bar which connects  $C_{S,n}$  to  $C_1$  is called  $Z_P$ . The impedances of the passive components given in Tab. I were measured via a programmable LCR-Bridge. According to datasheet, the LCR Bridge has a measuring range of

- 0,01 m $\Omega$  to 100 M $\Omega$  for resistive load,
- 0,01 pF to 100 mF for capacitive load,
- 10 nH to 100 kHz for inductive load.

The frequency ranges from 20 Hz up to 100 kHz. Measurement is done via four-wire measurement. Results presented were obtained at a measurement signal frequency of 100 Hz.

To measure the current  $i_E$ , three clamp-on probes are applied to the test bench. According to datasheet, the bandwidth of these probes ranges from DC to 10 MHz. The amplitude accuracy is stated  $\pm 1\%$  of reading. The rise time is stated to be 35 ns or less. For the current  $i_E$  during the switching action presented in Fig. 10 this means a phase accuracy of only 65%.  $i_E$  contains high frequency components due to the VSC switching transients. Correct measurement data acquisition of the clamp-on probes for those high frequency distortions is validated. For this purpose, a comparative measurement is performed using a Rogowski coil with an HF bandwidth of 30 MHz. The stated maximum current rise that can be detected is  $20 \text{ kA } \mu\text{s}^{-1}$ . The results of the comparison measurement between Rogowski coil ( $i_{DC,V,\sim}$ ) and clamp-on probe ( $i_{DC,V}$ ) are shown in Fig. 10 presenting DC-side currents for phase V during one switching action of the DUT. It can be seen that the transient effect is similar for both probes proving the bandwidth of the clamp-on probe is sufficient. Fig. 10 also shows the voltage overshoot  $u_{CC,V}$  caused by the impedance  $Z_{R,V}$  which has to be kept as low as possible to avoid damage to the IGBT modules of the DUT. Compared to the collector emitter saturation voltage of 1200 V stated in the data sheet of the DUT, the measured voltage overshoot is reasonable.

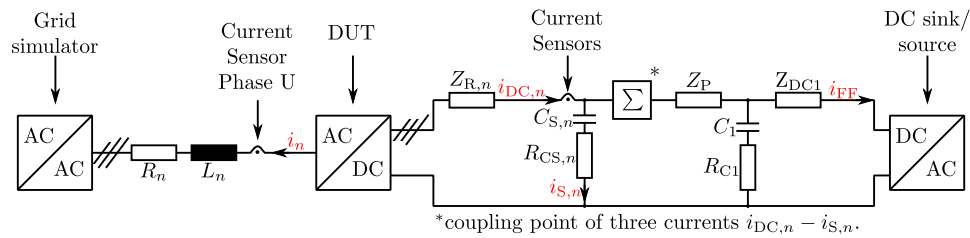


Figure 8: Schematic of the test bench used for verification of the calculated results.

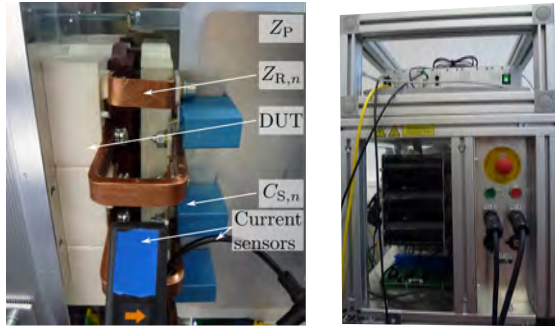


Figure 9: Coupling of the VSC and its DC-link for measurement of  $i_E$  (left picture). Experimental set-up of VSC used as DUT (right picture).

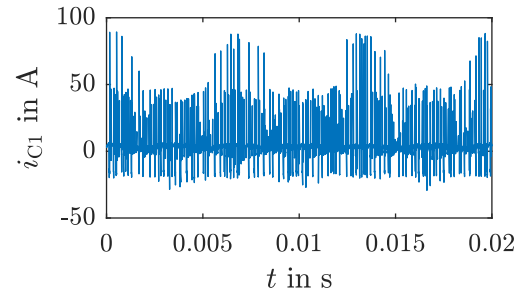


Figure 11: Measured capacitor current over one fundamental period of 20 ms.

In Fig. 11, also the measurement results of the capacitor current  $i_C$  over one fundamental period of 20 ms is shown. As  $i_C$  can not be measured directly, it is calculated from the AC parts  $i_{DC,n\sim}$  of the currents  $i_{DC,n}$  with  $n = U, V, W$  as stated in (36). The operating point for the measurement is  $\varphi = 0^\circ$ ,  $m_a = 1$ .

$$i_C = i_{DC,U\sim} + i_{DC,V\sim} + i_{DC,W\sim} \quad (36)$$

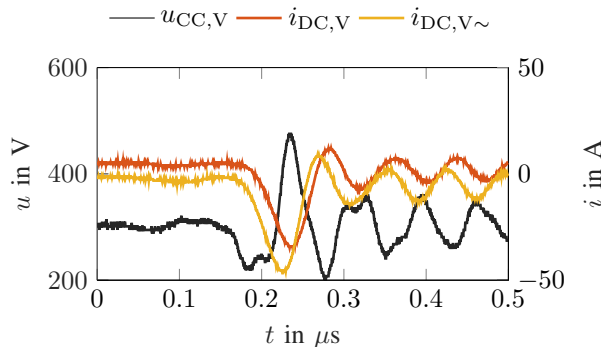


Figure 10: Comparative current measurement between Rogowski coil and clamp-on probe, measured in phase V. DC-side current and voltage during one switching action of the DUT.

Fig. 12 shows the comparison of results.

- Results from calculation method presented:  $K_{DC,analyt}$ .
- Unfiltered measurement:  $K_{DC,meas}$ .
- Filtered measurement:  $K_{DC,f}$ .

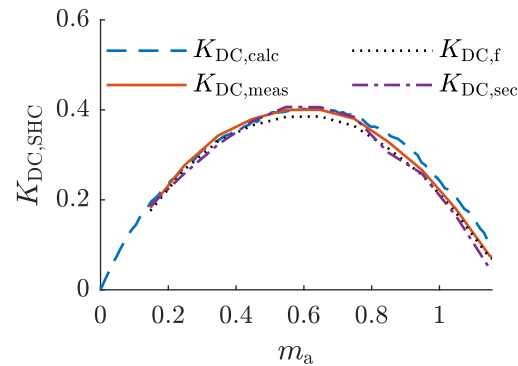


Figure 12: Comparison of measured test bench results with calculation results.

#### A. Transient effects

To minimize the distortion in the measurement caused by the necessary hardware intervention as described, the course of  $K_{DC,SHC}$  was additionally determined with a filtered current signal of  $i_E$ . In Fig. 13 the unfiltered current at operating point  $m_a = 1$  is shown. Fig. 13 also shows the filtered current, which is used for computing  $K_{DC,f}$  as seen in Fig. 12. For filtering purpose, a first order low pass with a cut off frequency of 5 MHz is used. As expected, the filtered-value of  $K_{DC,SHC}$  is lower than the calculated one using the unfiltered

current  $i_E$  over the entire course. Especially in the middle of the modulation range,  $K_{DC,SHC,f}$  is also lower than the results determined by calculation or simulation, respectively. Considering these results, subsequent filtering does not give an advantage compared to accepting the additional distortion caused by the hardware intervention.

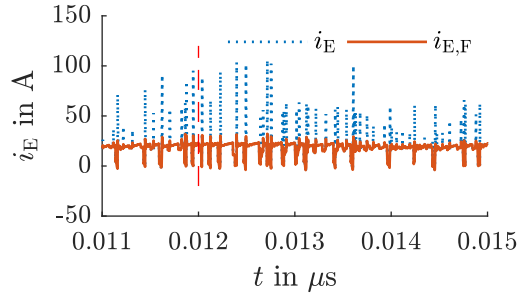


Figure 13: Comparison of the unfiltered current  $i_E$  with the filtered current  $i_{E,F}$ .

### B. Current commutation

This issue is already encountered in section IV by comparing calculated results with those from nonideal simulation. The deviation arising from this can be calculated on the basis of different relative switch-on times of the active SVs  $\delta_a$  or the ZVV  $\delta_0$ . In addition, the current error changes during the commutation process due to the commutation current. This results in a shift of the switch-on times of the SV required by the controller. The correlations between modulation level and relative switch-on time can be depicted for  $\varphi = 0^\circ$  as follows:

$$\lim_{m_a \rightarrow 0} \delta_0 = 1 \quad (37)$$

$$\lim_{m_a \rightarrow 2/\sqrt{3}} \delta_0 = 0 \quad (38)$$

If the phase currents  $i_n$  are set equal to its RMS value  $I_n$  and  $I_n$  set equal for all three phases ( $I_n = I_N$ ), the relative on times of the active space vectors can be summed up to one common relative on time for all active space vectors  $\delta_a$ . Accepting these simplification, the normalized distortion current load factor of the DC-link can be recalculated to

$$K_{DC}(i_n = I_N) = \frac{\delta_a I_N^2 - (\delta_a I_N)^2}{I_N^2} \quad (39)$$

with  $1 - \delta_a = \delta_0$

$$K_{DC}(i_n = I_N) = \delta_0 \cdot \delta_a$$

Due to the definition of  $K_{DC}(i_n = I_N)$  and the relations between  $\delta_0$  and  $m_a$  it becomes clear that deviations of the relative switch-on times are particularly noticeable at the limits of the modulation range and have a significant impact on the result.

Fig. 14 shows the results of  $K_{DC}(i_n = I_N)$  for calculation and measurement. The results prove, the visible deviations for  $m_a > 0.8$  and  $m_a < 0.3$  can be explained by the neglect of the current commutation process time  $t_D$  for the calculation method presented.

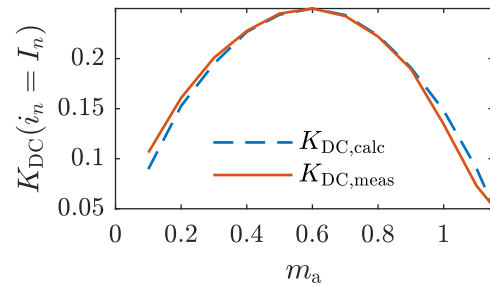


Figure 14: Comparative result of  $K_{DC}(i_n = I_N)$  for calculation ( $K_{DC,calc}$ ) and measurement ( $K_{DC,meas}$ ).

### C. Stationary current error

SHC remains a stationary error in its AC currents  $i_n$ . The phenomenon of remaining error is a known issue for hysteresis control, discussed for DC-values in [15]<sup>3</sup>. The calculation method presented considers this issue. But, mainly caused by  $t_D$ , the stationary current error of the test bench results differs from calculated results. Based on the observed deviations the RMS value of the AC-side current  $I_N$  is measured by a current probe instead of being calculated from the set current.  $I_N$  is needed to compute the measured curve of  $K_{DC,SHC}$ .

### D. VSC and filter voltage drop

The calculation method presented does not take into account current dependent voltage drop on the AC-side filter as well as the voltage drop  $u_{CE}$  of the DUTs IGBT modules: To consider the voltage drops of the real system, the modulation level  $m_{a,meas}$  is calculated as stated in (40). The value for  $u_{CE}$  is taken from the corresponding data sheet of the power module and is set to  $u_{CE} = 1,7\text{V}$  for evaluation.

$$m_{a,meas} = \frac{2\hat{e}_N}{u_{DC} - 2u_{CE} - 2R_N I_N} \quad (40)$$

### E. Voltage sector selection

In [12]<sup>4</sup>, it is stated that the SHC method depends on reliable information regarding the position of  $\underline{u}'_{\alpha\beta}$  in order to ensure correct sector selection. In particular, the change of the sector serving as the basis for the SV selection presents a challenge. Because of this, the sensor-less acquisition of  $\underline{u}'_{\alpha\beta}$  for the purpose as pilot-control of the SHC method was described in [16]<sup>5</sup>. Both in the implementation on the test bench and in the simulation model, the method developed in the framework of [16] is used for pilot-control of the SHC method. To hide the influence of sector transitions the filtered measurement result is computed by considering sections of  $54^\circ$  in the middle of the  $60^\circ$  sectors. This result is named  $K_{DC,sec}$  in Fig. 12. The result shows only a slight difference in distortion current load factor, which confirms the results of precise sector transitions described in [16].

<sup>3</sup>Chapter 3, p.182 et seq.

<sup>4</sup>Chapter 5, page 100.

<sup>5</sup>Chapter 4, page 63 et seq.

## VI. ACCURACY IN COMPARISON TO STATE-OF-THE-ART METHODS

In [2] for  $\varphi = 0^\circ$  and  $0 \leq m_a \leq 1,15$  the average error  $\epsilon$  between calculated and measured results is stated to be about

- $\epsilon = 5\%$  for low AC ripple current ( $\kappa = 0, 1$ ) and
- $\epsilon = 9\%$  for high AC ripple current ( $\kappa = 0, 8$ ).

The relative amplitude of the AC side ripple current for pulse-width-modulated VSCs is calculated in [2] as follows:

$$\kappa = \frac{1}{\hat{I}_N} \cdot \frac{U_{DC} T_P}{8L_N} \quad (41)$$

In order to keep the absolute amplitude of the AC side ripple current constant using the direct current controller SHC, the mean switching frequency is not constant over the modulation level. Instead, the switch-on time  $t_{SV}$  is adjusted:

$$\frac{U_{DC} t_{SV}}{8L_N} = 8I_\epsilon \quad (42)$$

The maximum error current is set to  $I_\epsilon = 1$  A. Applied to the relative ripple current as stated in [2],  $\kappa$  can be calculated as follows:

$$\kappa = \frac{I_\epsilon}{\hat{I}_N} \quad (43)$$

The relative error between measurement and calculation is

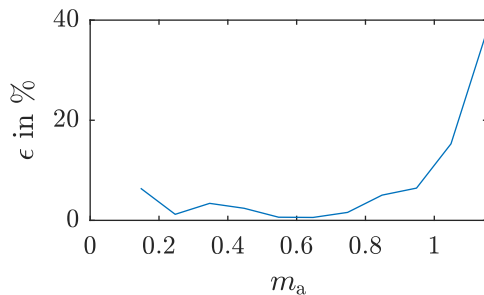


Figure 15: Relative error of the calculated results in comparison to experimental results.

shown in Fig. 15 for  $\varphi = 0^\circ$  and  $0 \leq m_a \leq 1,15$ . It shows an accuracy of better than 8% for  $m_a < 0,9$ . The lower relative accuracy for higher modulation levels can be traced back to the neglect of the current commutation process as stated in section V. For the experimental set-up,  $I_N = 20$  A resulting  $\kappa = 0,4$ . The mean average error  $\epsilon = 7,3\%$ . From simulation results in [2] it can be seen that the error goes nearly linear with  $\kappa$ . Assuming this, the error of [2] would be 6,7% at  $\kappa = 0,4$  which is quite close to the error of the proposed method. This shows, with regard to accuracy the results for the method proposed for direct current controlled VSCs are comparable to state of the art methods for pulse width modulated VSCs.

## VII. CONCLUSION AND FUTURE WORK

A calculation scheme for determining the DC-link capacitor RMS current load for direct current control methods is presented. As an example, the approach is applied to the Scalar Hysteresis Control, a direct current control algorithm operating in the  $\alpha\beta$  plane.

As a reference, the DC-link capacitor RMS current load for SVM  $K_{DC,SVM}$  is calculated using state of the art methods. The comparison between results for SVM and SHC shows a striking similarity over the whole operation area as shown in Fig. 6. This can be justified by the identical sector-dependent SV selection and indicates that, even with no fixed pulse period, the behaviour of SHC is very similar to the behaviour of SVM. As SVM is considered to exactly adjust the set voltage, slight deviations can be traced back to the stationary current error of SHC.

The calculated results for  $K_{DC,SHC}$  are verified by digital simulation and test bench measurements and show good correlation. The post treatment of the measurement results are explained. These are:

- Filtering of transient effects caused by the necessary hardware intervention for measurement.
- Current commutation process not considered in the calculation method presented.
- Stationary current error of direct current controllers.
- IGBT/Diode voltage drop causing need for recalculation of  $m_a$ .
- Voltage sector selection using pilot-control for SHC.

With the pilot-control described in section V-E the influence of voltage sector selection is negligible. By comparing Fig. 14 and Fig. 12 it becomes clear that the remaining deviation between calculated and measured results can be addressed to the current commutation process. But as the behaviour of semi-conductors is dependent on many parameters, accounting this process in the generalized, hardware independent calculation method presented does not seem expedient.

Although, it is applied to a specific algorithm, the method presented is a general approach and can be applied to any direct current controller. In contrast to pure numerical simulation, the proposed method provides results in closed form expressions that are new and useful for the design/component development process.

The derivation of the calculation method presented analytically proves that the global RMS value of the DC-side input current  $I_E$  for the exemplary utilized Scalar Hysteresis Control (SHC) is independent of

- the radius of the tolerance area  $I_\epsilon$ , as well as of
- the AC-side filter components.

The calculation method presented does not determine the instantaneous DC current waveform like in numerical simulation. Determination of the instantaneous DC current waveform implicates calculation of the absolute on times. This causes high computation effort due to the very high frequency components and non-linearities of the instantaneous DC current waveform without any benefit for the RMS value calculation. Instead, the calculation method presented calculates the normalized distortion current load factor  $K_{DC}$  by only determining the relative on times. This causes very less computation effort and therefore is a great advantage of the calculation method presented compared to numerical simulation (approximately 570 times faster).

Even though, the paper presented focuses on calculation of the DC-link capacitor current load, preliminary work is done

for calculating the capacitor ripple voltage of direct current controlled VSCs. This refers to the determination of total on times in section III-A needed for calculating the capacitor ripple voltage according to the generic approach as stated in (5). This issue will be focussed in future work.

## REFERENCES

- [1] S. Piepenbreier, J. Berlinecke, N. Burani, R. Bittner, S. Matichyn, F. Streit, M. Hofmann, and R. Plikat, "Analysis of a multiphase multi-star pmsm drive system with sic-based inverter for an automotive application," in *PCIM Europe 2018; International Exhibition and Conference for Power Electronics, Intelligent Motion, Renewable Energy and Energy Management*. V, 2018, pp. 1 – 10.
- [2] J. W. Kolar and S. D. Round, "Analytical calculation of the rms current stress on the dc-link capacitor of voltage-pwm converter systems," *IEEE Proceedings - Electric Power Applications*, vol. 153, no. 4, p. 535, 2006.
- [3] B. Basler, T. Greiner, and P. Heidrich, "Reduction of dc link capacitor stress for double three-phase drive unit through shifted control and phase displacement," in *2015 IEEE 11th International Conference on Power Electronics and Drive Systems*, 2015, pp. 887–889.
- [4] A. M. Hava, R. J. Kerkman, and T. A. Lipo, "Simple analytical and graphical tools for carrier based pwm methods," in *PESC97. Record 28th Annual IEEE Power Electronics Specialists Conference. Formerly Power Conditioning Specialists Conference 1970-71. Power Processing and Electronic Specialists Conference 1972, 22-27 June 1997*, pp. 1462–1471.
- [5] E. Un and A. M. Hava, "Performance analysis and comparison of reduced common mode voltage pwm and standard pwm techniques for three-phase voltage source inverters," in *Twenty-First Annual IEEE Applied Power Electronics Conference and Exposition, 2006. APEC '06*, March 19, 2006, pp. 303–309.
- [6] —, "A near-state pwm method with reduced switching losses and reduced common-mode voltage for three-phase voltage source inverters," *IEEE Transactions on Industry Applications*, vol. 45, no. 2, pp. 782–793, 2009.
- [7] B. A. Welchko, "Analytical calculation of the RMS current stress on the DC link capacitor for a VSI employing reduced common mode voltage PWM," in *2007 European Conference on Power Electronics and Applications*. IEEE, 2007.
- [8] P. Dahono, Y. Sato, and T. Kataoka, "Analysis and minimization of ripple components of input current and voltage of PWM inverters," *IEEE Transactions on Industry Applications*, vol. 32, no. 4, pp. 945–950, 1996.
- [9] Felix Jenni, Dieter Wüest, *Steuerverfahren für selbstgeführte Stromrichter*. Zürich Stuttgart: Vdf, Hochsch.-Verl. an der ETH Zürich Teubner, 1995.
- [10] D. Wüest and F. Jenni, "Space vector based current control schemes for voltage source inverters," in *Proceedings of IEEE Power Electronics Specialist Conference - PESC '93*. IEEE, 1993.
- [11] H. Wießmann, "Hochdynamisches direktes stromregelverfahren für pulswechselrichter im vergleich zu pwm-verfahren," Ph.D. dissertation, Universität Erlangen-Nürnberg, 2011.
- [12] M. Schaefer, "Direct current control for grid connected multilevel inverters," Ph.D. dissertation, Universitat Politècnica de Catalunya. Departament d'Enginyeria Elèctrica, 2017.
- [13] M. Schaefer, W. Goetze, M. Hofmann, F. Bayer, D. Montesinos-Miracle, and A. Ackva, "Direct current control for grid-connected diode-clamped inverters," *IEEE Transactions on Industrial Electronics*, vol. 64, no. 4, pp. 3067–3074, apr 2017.
- [14] S. S. Joachim Holtz, "A predictive controller for the stator current vector of ac machines fed from a switched voltage source," *IPEC Tokyo*, 1983.
- [15] H. Unbehauen, *Regelungstechnik II*. Vieweg+Teubner Verlag, 2009. [Online]. Available: [https://www.ebook.de/de/product/6475589/heinz\\_unbehauen\\_regelungstechnik\\_ii.html](https://www.ebook.de/de/product/6475589/heinz_unbehauen_regelungstechnik_ii.html)
- [16] M. Hofmann, "Improved control for multilevel inverters in grid applications," Ph.D. dissertation, Universitat Politècnica de Catalunya. Departament d'Enginyeria Elèctrica, 2018.